



Discussion

Fast and robust three-dimensional fluorescence source reconstruction based on separable approximation and adaptive regularization

Zhenwen Xue^a, Chenghu Qin^a, Qian Zhang^b, Xibo Ma^a, Xin Yang^a, Jie Tian^{a,b,*}^a Intelligent Medical Research Center, Institute of Automation, Chinese Academy of Sciences, Beijing 100190, China^b Life Sciences Research Center, School of Life Sciences and Technology, Xidian University, Xi'an 710069, China

ARTICLE INFO

Article history:

Received 5 February 2012

Received in revised form

26 July 2012

Accepted 20 August 2012

Available online 5 September 2012

Keywords:

Fluorescence molecular tomography

Inverse problem

Separable approximation

Adaptive regularization

ABSTRACT

In this study, a fast and robust reconstruction method based on the separable approximation and the adaptive regularization is presented for fluorescence molecular tomography. The subproblems can be established and solved efficiently through separable approximation, and the convergence process can be also accelerated by adaptive regularization. As is well known, the regularization parameter has an important impact on the results, and finding the optimal or near-optimal regularization parameter automatically is an challenging task. To solve this problem, the regularization parameter in the proposed method is updated heuristically instead of being determined manually or empirically. This adaptive regularization strategy of the proposed method can perform accurate reconstruction almost without worrying about the choice of the regularization parameter. By contrast, improper choice of the regularization parameter may cause larger location errors for the three contrasting methods. The proposed method is proved robust and insensitive to parameters, which can improve the reconstruction accuracy. Moreover, the proposed method was about 1–2 orders of magnitude faster than the contrasting methods commonly used in fluorescence tomography reconstruction. Furthermore, reliable performance on different initial unknown values and different noise levels was also investigated. Finally, the potential of the proposed method in a practical application was further validated by the physical experiment with a mouse model.

© 2012 Elsevier B.V. All rights reserved.

1. Introduction

In recent years, optical molecular imaging has attracted increasing attention due to its ability of non-invasive visualization of molecular and cellular processes [1–3]. As an important optical molecular imaging modality, fluorescence molecular tomography (FMT) is known for its cost-effectiveness and exquisite sensitivity [4–7]. FMT attempts to reconstruct the 3D spatial distribution of the fluorescent probes inside of small animals based on the photon propagation model, the anatomical structure information, the associated tissue optical properties, and the excitation power and position. Lots of efforts have been made to develop photon migration models [8,9], imaging systems [10–12] and reconstruction strategies [5,13,32,33]. For instance, in [32], data compression has been proved efficient in implementing fast reconstruction in FMT.

As we all know, only the light distribution on the surface is measurable, which makes the number of measurements is much

less than the number of unknowns. Therefore, the reconstruction of FMT is usually ill-posed [5]. Therefore, various regularization methods have been applied to make the solution stable and insensitive to noise. For example, the L2-norm constraint has been added to the original problem to improve the stability of optical tomography [14]. However, L2-norm regularization often makes the solution over-smoothed and results in a loss of localized features during reconstruction [16]. Hence, the L2-norm regularization strategy has difficulty obtaining a sparse solution in tomographic reconstruction.

Over the past few years, sparse regularization has been developed in the field of compressed sensing (CS) for signal and image processing. On the basis of the theory of CS, a sparse or compressive signal can be recovered from far fewer samples or measurements [15]. Coincidentally, in the practical application of FMT, the fluorescent sources which indicate the locations of tumor cells are usually small and sparse during early detection. Consequently, it is suitable to apply the CS theory to the FMT problem for recovering the fluorescent yield distribution. Inspired by the CS theory, several algorithms incorporated with L1-norm regularization have been proposed for solving optical tomography problems [4,16–18,34]. For example, in [17], an iterated-shrinkage-based (IS) algorithm for

* Corresponding author at: Intelligent Medical Research Center, Institute of Automation, Chinese Academy of Sciences, Beijing 100190, China.
E-mail address: tian@ieee.org (J. Tian).

the FMT reconstruction was proposed. It is reported to be effective in reducing the computational burden of the FMT reconstruction. However, it is a first order method and only has a linear convergence rate [19]. Therefore, a large number of iterations are required to obtain satisfactory results. A fast iterated shrinkage method (FIS) [20], as the accelerated version of the LS method, was proposed to reduce the number of iterations required for reconstruction. Similar to the iteration-shrinkage-based methods, Bregman iteration algorithms are efficient in solving L1-norm reconstruction problem [34]. It also can be seen as one of the state-of-the-art methods to solve optical tomographic problems. However, the regularization parameter of the LS, FIS and Bregman methods keeps unchanged and needs to be manually optimized. For FMT reconstruction, the regularization parameter has a significant impact on results: a large regularization parameter can cause large reconstruction errors, while a small one slows down the convergence process and may also cause location errors [17,21]. Therefore, an adaptive and robust strategy to choose the optimal or near-optimal regularization parameter is needed.

In this contribution, we propose a fast and robust reconstruction method based on the separable approximation and adaptive regularization to solve the FMT problem. Due to the separable approximation and the adaptive regularization strategy, the proposed method has a much higher convergence rate than the contrasting methods. The regularization parameter of the proposed method is updated adaptively instead of being manually optimized or estimated in advance empirically. Numerical experiments in Section 3.1 have demonstrated that improper choice of regularization parameter may reduce the reconstruction accuracy for the three contrasting methods, while the proposed method will almost not be affected and still able to achieve accurate reconstruction. The proposed method has been proved robust and insensitive to parameters. Numerical experiments also demonstrated that the proposed method was about 1–2 orders of magnitude faster than the contrasting methods.

The paper is organized as follows. In Section 2, the diffuse approximation model and the proposed algorithm are presented. Section 3 shows validations for the proposed algorithm using a mouse-mimicking heterogeneous phantom. In Section 4, an in vivo experiment is used to further validate our method. Finally, we discuss and conclude this paper.

2. Methods

2.1. Photon propagation model

The diffusion equation is usually used for depicting the near infrared photon propagation in the biological tissue. For steady-state FMT with the point excitation sources, the following coupled diffusion equations have been extensively used to depict photon propagation

$$\begin{cases} \nabla(D_x(r)\nabla\Phi_x(r)) - \mu_{ax}(r)\Phi_x(r) = -\Theta_s\delta(r-r_l) \\ \nabla(D_m(r)\nabla\Phi_m(r)) - \mu_{am}(r)\Phi_m(r) = -\Phi_x(r)\eta\mu_{af}(r) \end{cases} \quad (r \in \Omega) \quad (1)$$

where subscripts x and m denote the excitation and emission wavelengths respectively. $\Phi_{x,m}$ denotes the photon flux density. $\mu_{ax,am}$ is the absorption coefficient and $D_{x,m}$ is the diffusion coefficient in biological tissues. $\eta\mu_{af}(r)$ denotes the fluorescent yield distribution to be reconstructed. r_l represents the different locations of the point sources with an amplitude of Θ_s . To solve these equations, the Robin-type boundary conditions are added on the boundary $\partial\Omega$ of the domain Ω [22]

$$2D_{x,m}\partial\Phi_{x,m}/\partial\vec{n} + q\Phi_{x,m} = 0 \quad (2)$$

where \vec{n} represents the outward normal vector to the surface. q is a constant depending on the optical reflective index mismatch at the boundary.

The finite element method has been applied in solving the diffusion equations. We discretize the domain with tetrahedrons and take the basic functions as the test functions. Then, the matrix form equations are obtained as

$$[K_x]\{\Phi_x\} = \{S_x\} \quad (3)$$

$$[K_m]\{\Phi_m\} = [G]\{X\} \quad (4)$$

where K_x is the system matrix during excitation, while K_m and G are matrices in emission. S_x represents the excitation source distribution after discretization. For each excitation point source at r_l , Φ_x can be obtained by solving Eq. (3). X denotes the fluorescent yield distribution to be reconstructed. Considering that K_m is symmetrical positive matrix, Eq. (4) can be changed into

$$\{\Phi_{m,l}\} = [K_{m,l}^{-1}][G_l]\{X\} = [D_l]\{X\} \quad (5)$$

By removing the immeasurable entries in $\Phi_{m,l}$ and the corresponding rows in D_l , we have

$$\{\Phi_{m,l}^{meas}\} = [A_l]\{X\} \quad (6)$$

For simplification, let Φ denotes $\Phi_{m,l}^{meas}$ and A denotes A_l . Then the linear relationship between the emitted fluorescence measurements Φ on the surface and the unknown fluorescent yield distribution X can be established as follows:

$$AX = \Phi \quad (7)$$

More details can be found in [5].

2.2. The proposed algorithm

As mentioned earlier, the tumors are often small and sparse during early detection, so the fluorescent sources that indicate the distribution of tumors are sparse as well. This can be considered as a type of a priori information. The L1-norm regularization has been increasingly used in optical tomography for its ability to promote the sparsity of the solution. The L1-norm regularization is incorporated in the FMT problem to increase the sparsity constraint, and Eq. (7) is transformed into an optimization problem

$$\min_X E(X) = F(X) + \lambda\|X\|_1 \quad (8)$$

where λ is the regularization parameter and $F(X) = \|AX - \Phi\|_2^2$. $F(X)$ can be expanded and reformulated as follows:

$$F(X) \approx F(X^k) + (X - X^k)^T \nabla F(X^k) + \frac{1}{2}(X - X^k)^T \nabla^2 F(X^k)(X - X^k) \quad (9)$$

Eq. (9) can be viewed as a quadratic separable approximation to $F(X)$ about X^k . When $\alpha_k I$ is used to mimic the Hessian $\nabla^2 F(X)$, and the constant term $F(X^k)$ is omitted, the following subproblem can be set up and solved at each iteration [24]

$$X^{k+1} = \arg\min_X (X - X^k)^T \nabla F(X^k) + \frac{\alpha_k}{2}\|X - X^k\|_2^2 + \lambda\|X\|_1 \quad (10)$$

I is the unit matrix. An equivalent form [23] of Eq. (10) is

$$X^{k+1} = \arg\min_X \frac{1}{2}\|X - Z^k\|_2^2 + \frac{\lambda}{\alpha_k}\|X\|_1 \quad (11)$$

where

$$Z^k = X^k - \frac{1}{\alpha_k} \nabla F(X^k) \quad (12)$$

More details of the above form transformation can be found in [24].

Due to the separable form of the regularization term $\lambda/(\alpha_k)\|X\|_1$, the subproblem of Eq. (11) can be written as

$$x_i^{k+1} = \operatorname{argmin}_x \frac{(x - z_i^k)^2}{2} + \frac{\lambda}{\alpha_k} |x|, \quad i = 1, 2, \dots \quad (13)$$

For each specific x , the minimization in Eq. (13) has a unique solution which can be obtained by

$$\operatorname{argmin}_x \frac{(x - z_i^k)^2}{2} + \frac{\lambda}{\alpha_k} |x| = \operatorname{soft}\left(z_i^k, \frac{\lambda}{\alpha_k}\right) \quad (14)$$

where $\operatorname{soft}(w, a) = \operatorname{sign}(w) \max\{|w| - a, 0\}$ is the well-known soft-threshold function [25]. The simple diagonal Hessian approximation $\alpha_k I$ plays an important role for its ability to affect the accuracy and convergence rate of the problem. Here, the Barzilai–Borwein (BB) spectral approach [26] is introduced to determine α_k . It is required that $\alpha_k S^k = R^k$ in the least-square sense, hence

$$\alpha_k = \operatorname{argmin}_\alpha \| \alpha S^k - R^k \|_2^2 = \frac{(S^k)^T R^k}{(S^k)^T S^k} \quad (15)$$

where $S^k = X^k - X^{k-1}$ and $R^k = \nabla F(X^k) - \nabla F(X^{k-1})$.

The regularization parameter λ is usually a constant in state-of-the-art algorithms [17,34]. However, the convergence rate of the algorithm becomes low when λ is small, while there are larger reconstruction errors if λ becomes bigger [17,21]. Accordingly, we expect to find a way to guarantee both the accuracy and time-efficiency. If we start the iteration with a large value of λ , then decrease λ in steps toward its desired value, it may lead to a rapid global convergence. It is based on the consideration that when the solution is far from the true value, λ is set to a large value to accelerate the convergence process, and when the solution is closer to the true value, λ is set to a small value to obtain an accurate solution.

$\|A^T Y^k\|_\infty$ indicates that the current error is employed to specify the sequence of values for λ . Here, $Y^{k+1} = \Phi - AX^{k+1}$. The regularization parameter λ is defined as the maximum value of λ_{final} and $\zeta \|A^T Y^k\|_\infty$. At the beginning of the iteration, $\|A^T Y^k\|_\infty$ represents the level of reconstruction errors which has a large value. With the increase in the number of iterations, $\|A^T Y^k\|_\infty$ becomes smaller since the reconstruction errors are reduced. Consequently, relying on the changes in $\|A^T Y^k\|_\infty$, an adaptive strategy to specify the sequence of values of λ is achieved. Additionally, in Algorithm 2, when the changing rate of the number of non-zero items of unknowns in the two adjacent iterations is less than 0.01, the algorithm is terminated.

Algorithm 1. Main algorithm of the proposed algorithm.

$$X^t = 0, \quad Y^t = \Phi, \quad 0 < \zeta < 1, \quad 0 < \lambda < 1.$$

for $t = 1$ to t_{\max} **do**

 Compute the new regularization parameter: $\lambda_t = \max\{\zeta \|A^T Y^t\|_\infty, \lambda_{final}\}$.

 Solve subproblems: $X^{t+1} = f(\Phi, A, \lambda_t, X^t)$.

 Compute current residue: $Y^{t+1} = \Phi - AX^{t+1}$.
 $t = t + 1$

if $\lambda_t \leq \lambda_{final}$ **then**

 Stop.

end if

end for

Algorithm 2. Solving the subproblems.

for $k = 1$ to k_{\max} **do**

 Compute gradient: $\nabla F(X^k) = A^T (AX^k - \Phi)$.

 Compute: $Z^k = X^k - \frac{1}{\alpha_k} A^T (AX^k - \Phi)$.

for $i = 1$ to n (size of X^k) **do**

$x_i = \operatorname{soft}(z_i^k, \frac{\lambda_t}{\alpha_k})$.

end for

if stopping criterion reached **then**

 Return.

else

$S^k = X^k - X^{k-1}$.

$R^k = A^T (AX^k - AX^{k-1})$.

$\alpha_k = \frac{(S^k)^T R^k}{(S^k)^T S^k}$.

end if

end for

3. Numerical experiments

In this part, we employ the heterogeneous simulation experiments to demonstrate the performance of our algorithm. Fig. 1(a) shows a 3D view of the heterogeneous cylindrical phantom that we utilized. It was 20 mm in diameter and 20 mm in height. Fig. 1(b) shows the slice of the phantom in a $z=0$ plane. We used four different kinds of materials to denote the muscle (M), lungs (L), heart (H) and bone (B) respectively. Two fluorescent sources (S) to be reconstructed were placed in one lung while one fluorescent source was placed in the other lung. The optical properties we used are listed in Table 1 [27]. As is seen in Fig. 1(b), the black dots denote the different excitation light sources. The isotropic point sources were placed at one mean free path of photon transport beneath the surface in the $z=0$ plane. The emitted fluorescence can be only measured in a 160° field of view on the opposite side of the cylindrical phantom for each excitation location. The FEM method was employed to solve the forward model and the measurements on the boundary was obtained [28]. For the forward problem, the mesh consisted of 187,417 tetrahedral elements and 34,294 nodes. This heterogeneous phantom was discretized into 3430 nodes and 17,623 tetrahedral elements.

In this paper, to better evaluate the proposed method, we compared it to the IS, FIS and Bregman methods. Note that the second reconstruction strategy in these two contrast methods was adopted for it needed less reconstruction time than the first one. For the proposed method, we set $\lambda_{final} = 2e-5$. For the contrasting methods, the regularization parameter was also set at $2e-5$. For all methods, the maximum iteration number was set at 20,000, which was enough for most cases. In addition, the zero vector was used as the initial value. All three reconstruction algorithms were coded in Matlab and performed on a personal computer with 3.20 GHz Intel® Core™ i5-650 Processor and 4 GB RAM.

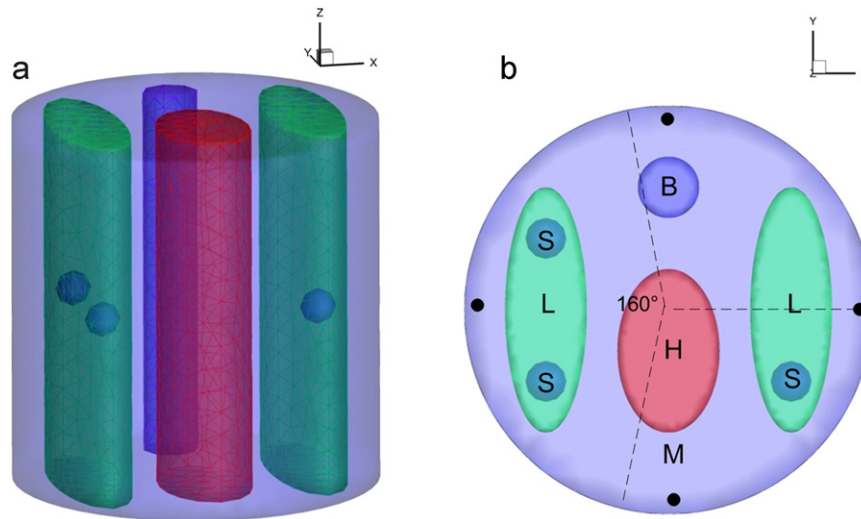


Fig. 1. Mouse-mimicking heterogeneous cylindrical phantom. (a) 3D view of the phantom with heterogeneous organs and fluorescent sources in it. (b) A slice image of the phantom in a $z=0$ plane. The excitation light source locations are represented by black dots. The emitted fluorescence can be only measured in a 160° field of view on the opposite side of the cylindrical phantom for each excitation location.

Table 1
Optical properties of the numerical phantom^a.

	μ_{ax}	μ_{am}	μ'_{sx}	μ'_{sm}
Muscle	0.0052	0.0068	1.08	1.03
Lungs	0.0133	0.0203	1.97	1.95
Heart	0.0083	0.0104	1.01	0.99
Bone	0.0024	0.0035	1.75	1.61

^a The unit for optical properties is mm^{-1} .

Table 2
Comparisons with different regularization parameters.

Sources	Location error (mm)							
	lambda_final	1e-4	1e-5	1e-6	1e-7	1e-8	1e-9	1e-10
S1	Proposed	0.28	0.28	0.28	0.28	0.28	0.28	0.28
	IS/FIS/Bregman	0.28	0.28	0.28	0.28	0.28	0.28	0.28
S2	Proposed	1.14	1.14	1.14	1.14	1.14	1.14	1.14
	IS/FIS/Bregman	1.14	1.14	1.69	1.69	1.69	1.69	1.69
S3	Proposed	0.54	0.54	0.54	0.54	0.54	0.54	0.54
	IS/FIS/Bregman	0.54	0.54	0.54	0.54	1.21	1.21	1.21

3.1. Reconstruction robustness to parameters

In this subsection, we validated the robustness of the proposed method to the regularization parameter. Comparisons with different λ_{final} can be seen in Table 2. The IS, FIS and Bregman methods all belong to state-of-the-art methods with L1-norm regularization and their regularization parameters keep unchanged throughout the reconstruction process. For the three contrasting methods, the regularization parameter is λ_{final} . They obtained similar reconstruction results with the same regularization parameters. With a decrease of λ_{final} (from $1e-4$ to $1e-10$), the reconstruction accuracy was not reduced. By contrast, the three contrasting methods could perform reconstruction accurately if the regularization parameter was selected appropriately. However, they may cause larger location errors when the regularization parameter was not estimated properly. When the regularization parameter was set less than $1e-6$, the location error of the second source increased from 1.14 mm to 1.69 mm by

48.2%. If the regularization parameter was estimated less than $1e-8$, the location error of the third source increased from 0.54 mm to 1.21 mm by 124.1%.

Based on the analysis above, we almost do not need to worry about proper choice of the regularization parameter in the proposed method. By contrast, improper choice of the regularization parameter may cause larger location errors for the IS, FIS and Bregman methods.

3.2. Convergence rate comparison

As seen in Fig. 2, all three methods obtained good reconstruction results. However, the proposed method only needed 150 iterations to obtain the desired reconstruction results, while the FIS method needed about 300 iterations, and the IS method needed more than 4000 iterations. We found that the IS method had a low convergence rate and needed a large number of iterations to obtain satisfactory results. Compared to the FIS method, which is the accelerated version of the IS method, the proposed method only needed half the number of iterations. Fig. 3 lists the iteration number comparisons of all three methods for four different grids. It demonstrates that the proposed algorithm has the lowest iteration number in all cases. For this point of view, the proposed method has obvious advantages in the convergence rate.

As previously described, the convergence rate of the algorithm becomes low when the regularization parameter λ is small, while it causes larger errors when λ becomes bigger. To obtain accurate reconstruction results, the regularization parameter of the two contrasting methods is set to a small value and is kept constant. Instead, the proposed method adopts an adaptive strategy to guarantee both the accuracy and efficiency by starting the iteration with a large λ , then decreasing it in steps toward a desired value. This is the key reason why the convergence rate of the proposed method is much higher than the two contrasting methods.

3.3. Efficiency studies for reconstruction

To better demonstrate the time-efficiency of the proposed method, we adopted four grids of different sizes to solve the FMT problem. To compare the reconstruction time of all the methods, we set the starting point at the time when Eq. (7) $AX = \Phi$ was just obtained. Each value was the average of ten independent runs. As seen in Table 3, the efficiency of the proposed method was about 1–2 orders of magnitude faster than the three contrasting methods.

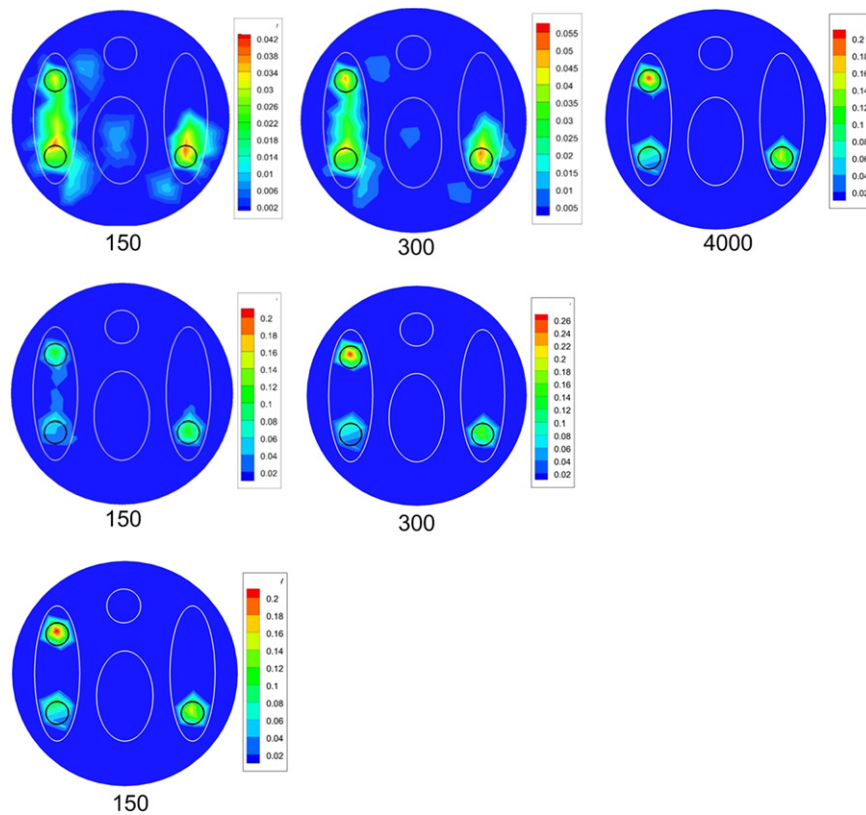


Fig. 2. Reconstruction comparisons with different iteration numbers. The iteration number from the left to the right column is 150, 300, and 4000 respectively. The reconstruction results from the top to the bottom row are from the IS method, the FIS method, and the proposed method respectively. The small circles in the lung regions in each cross section denote the real positions of the fluorescent sources.

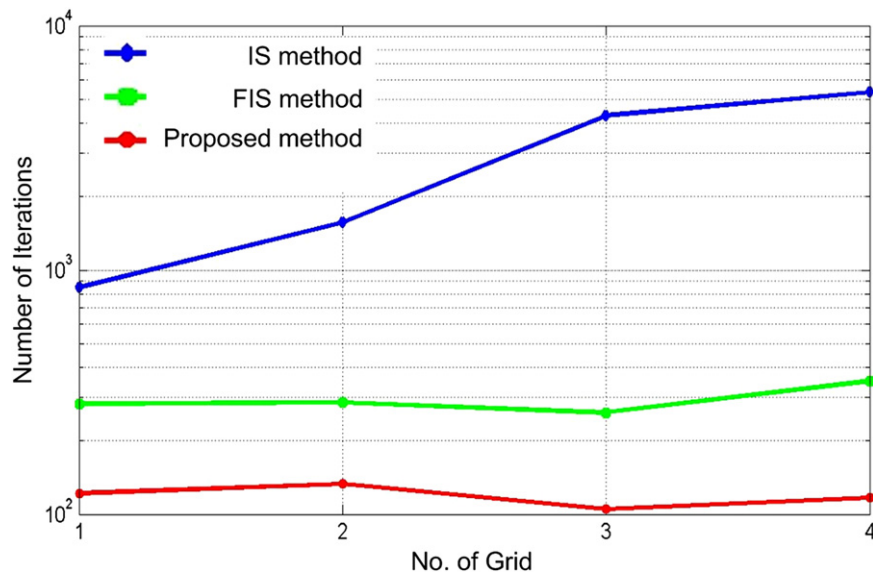


Fig. 3. Comparisons for the number of iterations needed for reconstruction.

Take the 3rd grid as an example, where the reconstruction time of the IS, FIS, Bregman method and proposed method were 69.94 s, 8.72 s, 9.32 s and 1.21 s respectively. It is founded that the efficiency predominance becomes larger with an increase in grid size.

3.4. Reconstruction robustness to initial unknowns

The reliability of the proposed algorithm was validated with different initial guesses for unknowns X . The initial guesses were

selected as 0, 1, 10, 100 respectively. As seen in Fig. 4, the fluorescent source distribution was reconstructed credibly, and the reconstruction results were hardly affected by the initial unknowns in all cases. To further demonstrate the reliability and tolerance of the proposed algorithm to different initial unknowns, we investigated the evolution values of $\|AX - \Phi\| / \|A^T \Phi\|$ with an increase in the iteration number. As seen in Fig. 5, note that no matter how large the initial unknowns were, the evolution values of $\|AX - \Phi\| / \|A^T \Phi\|$ nearly merged into one curve within about twenty iterations.

Table 3

Time efficiency comparisons of the reconstruction. The grid size means the number of points \times the number of elements.

No. of grid	1	2	3	4
Grid size	1232×6337	$2235 \times 11,468$	$3430 \times 17,623$	$4604 \times 23,866$
IS (s)	2.64	12.21	69.94	155.73
FIS (s)	1.24	3.53	8.72	18.08
Bregman (s)	1.42	3.87	9.32	20.35
Proposed (s)	0.25	0.75	1.21	2.53

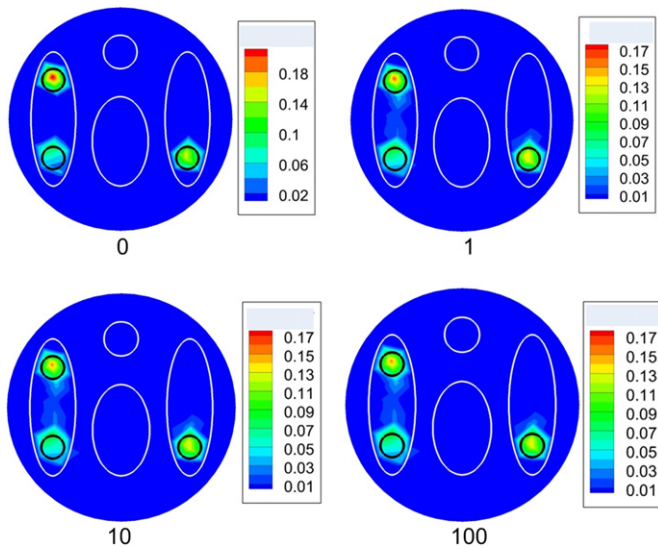


Fig. 4. Reconstruction results with different initial unknowns. The initials are 0, 1, 10, 100 respectively.

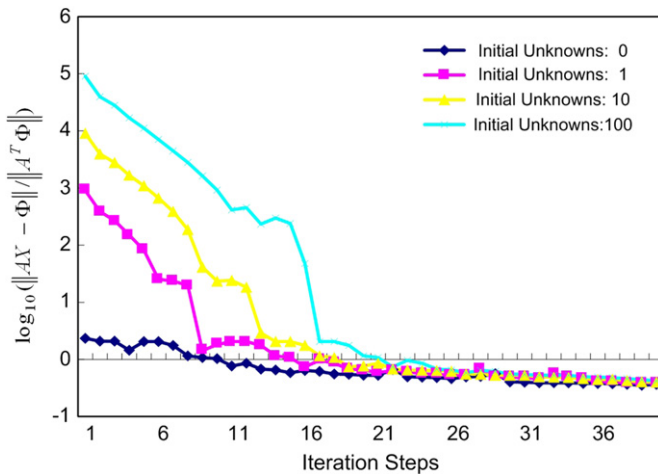


Fig. 5. The evolution curves as a function of iteration steps with different initial unknowns.

This indicated that the proposed algorithm was globally optimized and the results cannot be influenced by initial unknowns.

3.5. Reconstruction robustness to measurement of noise

To evaluate the stability and robustness of the reconstruction algorithm, we also considered the effects from noise. Additive Gaussian noise with different levels (5%, 10%, 30%, 50%) was added to the measured surface data. As seen in Fig. 6, even corrupted by 50% additive Gaussian noise, the proposed method

was able to recover the fluorescent sources accurately. In addition, the reconstruction time required for all noise levels was nearly the same. In other words, the proposed method is stable and robust to the interference of noise.

4. In vivo experiment

In this section, to further validate the proposed method, we employed an in vivo experiment on an adult BALB/C nude mouse. The experiment was performed on the dual-modality optical/micro-CT system [12,30]. The optical detector was a scientific CCD camera (VersArray, Princeton Instruments, Trenton, New Jersey) with the temperature cooled to -110°C . A bandpass filter with the center wavelength of 700 nm and the bandwidth of 10 nm was used to allow light transmission at the emission wavelength. The filter was made by float glass and quartz. Its optical density value at the excitation wavelength was larger than 5. The excitation light source was a 671 nm continuous wave laser with the output power of 22 mW and a laser spot diameter of 1 mm, which was small enough to simulate a point source case. The linewidth of the laser was less than 0.1 nm and the power stability was less than 5%@8 h. The fluorescent and background images can be seen in Fig. 7.

The main process of this in vivo experiment can be summarized as follows. We first injected the contrast agent Fenestra LC into the mouse with a tail vein injection, and then anesthetized the mouse using an intraperitoneal injection. Next, a bead filled with cy5.5 solution with a concentration of 2000 nM was implanted stereotactically into the body of the mouse in the vicinity of its liver. About forty minutes after the contrast agent injection, we placed the mouse on the rotating stage. First, 3D anatomical data was acquired using the micro-CT system and then the surface measurements of fluorescent signals were obtained. The fluorescence emitted from the surface of the mouse first passed through the bandpass filter, and was finally captured by the optical detector. In this experiment, we collected only one projection of the surface measurement data to perform reconstruction. The optical properties for different organs were calculated according to the literature [29] as listed in Table 4.

We used the finite element method to solve the inverse problem and did meshing on the segmented micro-CT data of the mouse. Due to the fact that different organs have different optical properties, we assigned a different number to a different organ in the meshing. Here, we did segmentation on six kinds of organs: muscle, lungs, heart, bone, liver, and kidneys. The mesh had 3053 nodes and 14,942 tetrahedral elements. After registering the fluorescence images and the volume data of the micro-CT, the surface energy mapping was carried out by using a 3D surface flux reconstruction algorithm [31], as is seen in Fig. 8. It took about 0.09 s to complete the reconstruction process using the proposed method. As seen in Fig. 9, two viewing angles (horizontal and vertical) have been employed to show the deviation of the actual source center. The actual source center was (20.35 mm, 21.22 mm, and 17.31 mm) while the reconstructed source center was (18.21 mm, 21.38 mm, and 17.68 mm), with a location error of 2.18 mm. This result is acceptable since the errors may have been caused by the diffusion equation model, the geometrical approximation, the optical properties inaccuracy, the surface energy mapping, and so on.

5. Conclusion

In this paper, we proposed a fast and robust method for the in vivo FMT reconstruction. The proposed method adopted the

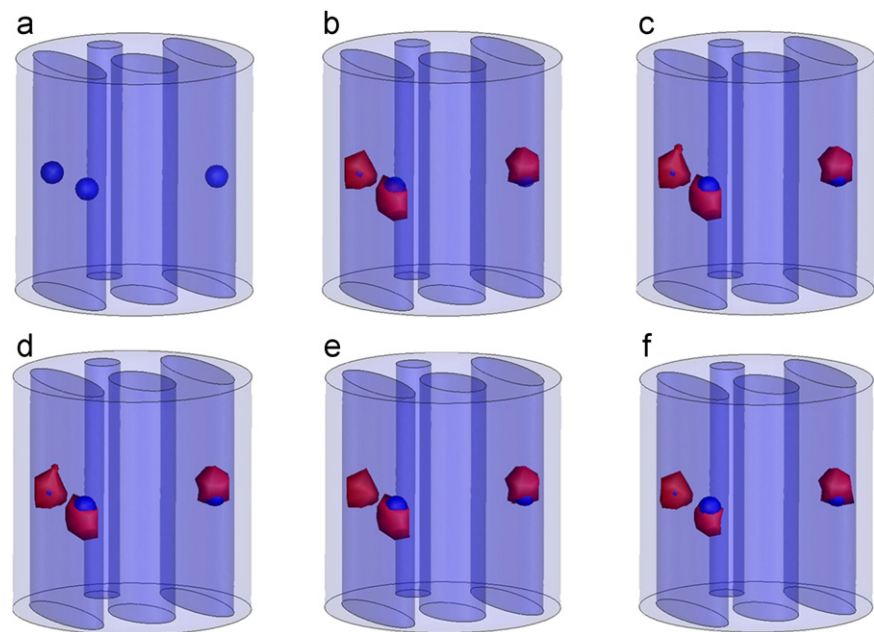


Fig. 6. Reconstruction results with fluorescence imaging measurements corrupted by different Gaussian noise levels using the proposed method. From (a) to (f), the spheres indicate the real locations of the fluorescent sources while the surfaces of the fluorescent sources are iso-surfaces for 30% of the maximum value. (a) Original locations of the fluorescent sources. (b) Reconstruction results without Gaussian noise. (c) 5% Gaussian noise. (d) 10% Gaussian noise. (e) 30% Gaussian noise. (f) 50% Gaussian noise. (For interpretation of the references to color in this figure legend, the reader is referred to the web version of this article.)

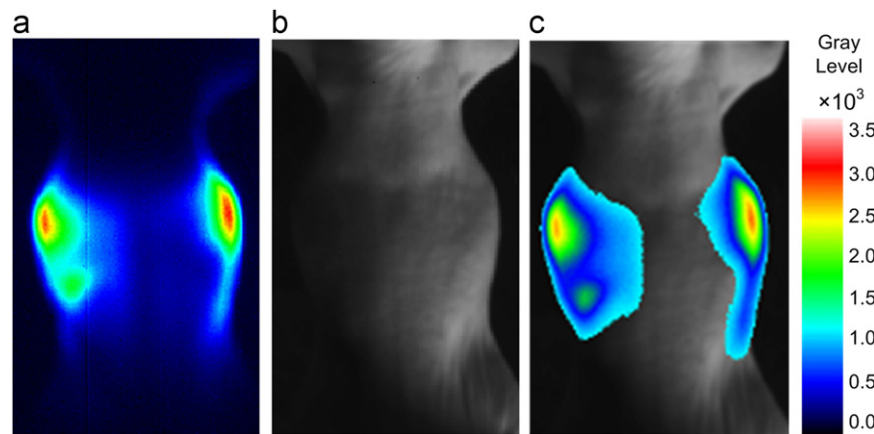


Fig. 7. Fluorescent and background images. (a) The fluorescent image. (b) The background image with white light. (c) The overlay of the fluorescent image and the background image.

Table 4
Optical properties of the mouse model^b.

Material	Muscle	Lungs	Heart	Bone	Liver	Kidneys
μ_{ax}	84.9	191.8	57.4	59.4	343.7	64.4
μ'_{sx}	427.3	2172.0	962.0	2490.0	677.0	2248.0
μ_{am}	56.3	126.6	38.3	39.3	228.3	43.0
μ'_{sm}	379.2	2124.0	905.0	2340.0	648.0	2109.0

^b The unit for optical properties is m^{-1} .

separable approximation to establish the subproblems which could be solved efficiently, and then used the adaptive regularization strategy to accelerate the convergence rate and maintain the reconstruction accuracy simultaneously. Both the numerical experiments and the physical experiment demonstrated the high efficiency of the proposed method, which was very suitable for the practical application of FMT.

The regularization parameter of the proposed method is updated heuristically, instead of being determined manually or empirically. The adaptive regularization strategy of the proposed method can perform accurate reconstruction almost without worrying about the choice of the regularization parameter. By contrast, improper choice of the regularization parameter may cause larger location errors for the IS, FIS and Bregman methods. The proposed method is proved robust and insensitive to parameters, which can improve the reconstruction accuracy.

We also performed the reconstructions with different initial unknown values and different noise levels. It is validated that the proposed method is globally optimized and can obtain satisfactory results in all test cases. Moreover, compared to the iteration-shrinkage-based methods, the proposed method had a higher convergence rate and needed a much lower iteration number. Consequently, the time-efficiency of the proposed method was about 1–2 orders of magnitude faster than the contrasting methods.

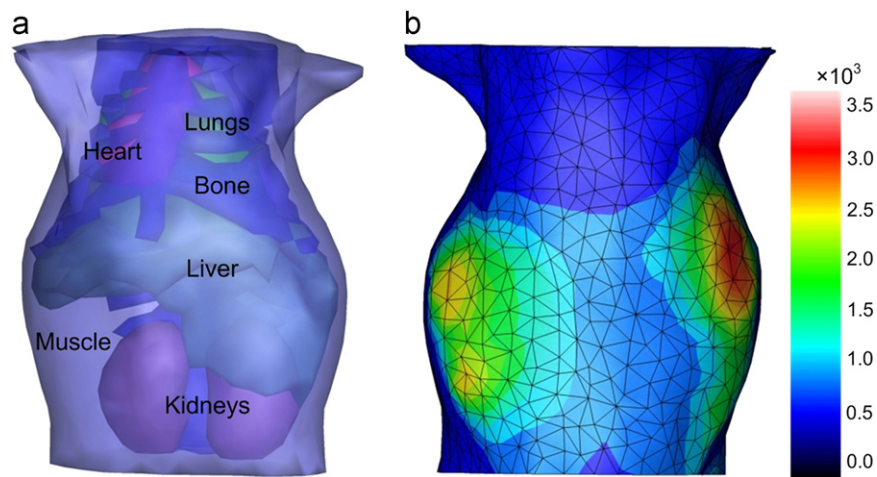


Fig. 8. In vivo experimental data in a 3D view of the organs and surface energy mapping. (a) 3D view of the segmented micro-CT data of the mouse with a source implanted beneath the liver. (b) The surface view of the reconstruction mesh with the measurement distribution mapping on it.

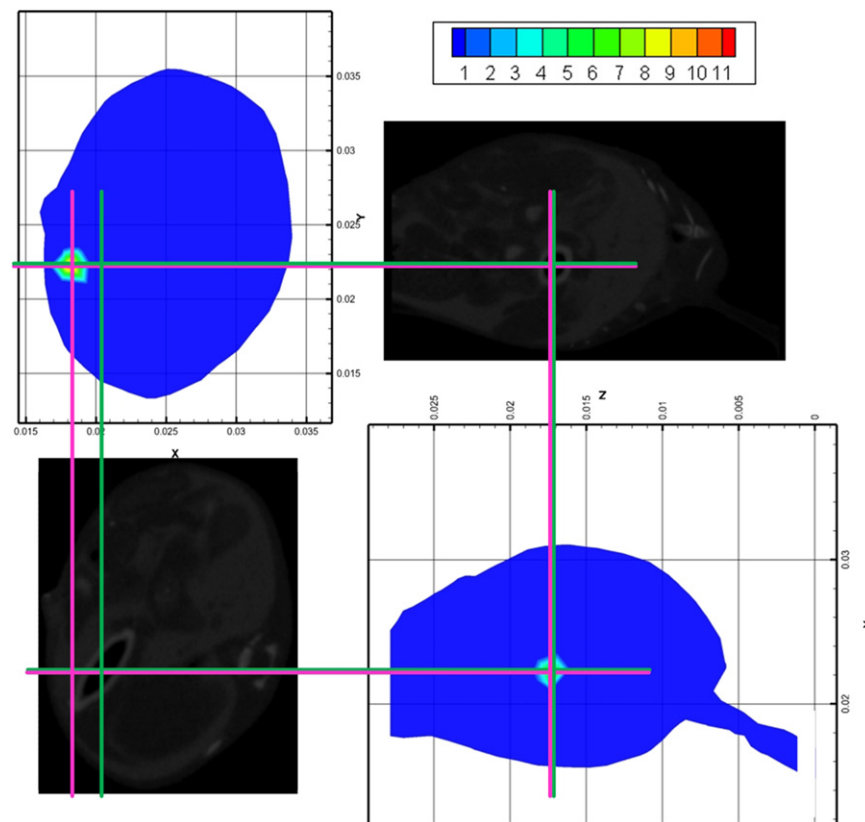


Fig. 9. The reconstruction results for the in vivo experiment. The cross section of the reconstruction results is compared to the corresponding CT slice. The cross of pink solid lines denotes the actual source center. The longitudinal section of the reconstruction results is compared to the corresponding CT slice. The cross of green solid lines denotes the actual source center. (For interpretation of the references to color in this figure legend, the reader is referred to the web version of this article.)

Although the diffusion approximation model for the FMT reconstruction is very popularly used, a more accurate model to describe the photon propagation in biological tissues is needed to enhance the quality of the 3D image reconstruction. The imaging system and the experimental procedures also need improvement. For example, if not properly tackled, the 3D surface energy mapping may cause large location errors. Furthermore, some organs have been ignored in the heterogeneous model for simplicity, as well as the optical properties inaccuracy, which will lead to reconstruction errors.

In conclusion, a fast and robust method based on the separable approximation and the adaptive regularization for the FMT

reconstruction has been presented. Both the numerical experiments and the in vivo experiment have validated the high efficiency and robustness of the proposed method. In future work, in vivo experiments with probe-marked models and more precise forward models will be developed.

Acknowledgments

This paper is supported by the National Basic Research Program of China (973 Program) under Grant no. 2011CB707700, the

Knowledge Innovation Project of the Chinese Academy of Sciences under Grant no. KGCX2-YW-907, the National Natural Science Foundation of China under Grant nos. 81027002, 81071205, 30970778, 81071129, 81101095, the Beijing Natural Science Foundation No. 4111004, the Science and Technology Key Project of Beijing Municipal Education Commission under Grant no. KZ200910005005, the Fellowship for Young International Scientists of the Chinese Academy of Sciences under Grant no. 2010Y2GA03, and the Chinese Academy of Sciences Visiting Professorship for Senior International Scientists under Grant no. 2010T2G36.

References

- [1] V. Ntziachristos, J. Ripoll, L.V. Wang, R. Weissleder, *Nature Biotechnology* 23 (2005) 313.
- [2] J.K. Willmann, N. van Bruggen, L.M. Dinkelborg, S.S. Gambhir, *Nature Reviews Drug Discovery* 7 (2008) 591.
- [3] X. Ma, J. Tian, X. Yang, C. Qin, S. Zhu, Z. Xue, *Acta Biophysica Sinica* 27 (2011) 355.
- [4] P. Mohajerani, A.A. Eftekhari, J. Huang, A. Adibi, *Applied Optics* 46 (2007) 1679.
- [5] X. Song, D. Wang, N. Chen, J. Bai, H. Wang, *Optics Express* 15 (2007) 18300.
- [6] Y. Tan, H. Jiang, *Applied Optics* 47 (2008) 2011.
- [7] F. Leblond, K.M. Tichauer, R.W. Holt, F. El-Ghoussein, B.W. Pogue, *Optics Letters* 36 (2011) 3723.
- [8] Y. Lu, B. Zhu, H. Shen, J.C. Rasmussen, G. Wang, E.M. Sevick-Muraca, *Physics in Medicine and Biology* 55 (2010) 4625.
- [9] J. Ripoll, V. Ntziachristos, *Modern Physics Letters B* 18 (2004) 1403.
- [10] V. Ntziachristos, G. Wang, *European Radiology* 13 (2003) 195.
- [11] G. Hu, J. Yao, J. Bai, *Progress in Natural Science* 18 (2008) 707.
- [12] C. Qin, S. Zhu, J. Tian, *Current Pharmaceutical Biotechnology* 11 (2010) 620.
- [13] X. Liu, F. Liu, Y. Zhang, J. Bai, *IEEE Transactions on Medical Imaging* 30 (2011) 1591.
- [14] W. Bangerth, A. Joshi, *Inverse Problems* 24 (2008) 034011.
- [15] D.L. Donoho, *IEEE Transactions on Information Theory* 52 (2006) 1289.
- [16] Y. Lu, X. Zhang, A. Douraghy, D. Stout, J. Tian, T.F. Chan, A.F. Chatziioannou, *Optics Express* 17 (2009) 8062.
- [17] D. Han, J. Tian, S. Zhu, J. Feng, C. Qin, B. Zhang, X. Yang, *Optics Express* 18 (2010) 8630.
- [18] N. Cao, A. Nehorai, M. Jacob, *Optics Express* 15 (2007) 13695.
- [19] M. Elad, B. Matalon, M. Zibulevsky, *Applied and Computational Harmonic Analysis* 23 (2007) 346.
- [20] D. Han, J. Tian, C. Qin, B. Zhang, K. Liu, X. Ma, *Proceedings of SPIE* 7965 (2011) 79651C.
- [21] E.T. Hale, W. Yin, Y. Zhang, TR07-07, Department of Computational and Applied Mathematics, Rice University, 2007.
- [22] M. Schweiger, S.R. Arridge, M. Hiraoka, D.T. Delpy, *Medical Physics* 22 (1995) 1779.
- [23] P.L. Combettes, V.R. Wajs, *Multiscale Modeling and Simulation* 4 (2006) 1168.
- [24] S.J. Wright, R.D. Nowak, M.A.T. Figueiredo, *IEEE Transactions on Signal Processing* 57 (2009) 2479.
- [25] D.L. Donoho, *IEEE Transactions on Information Theory* 41 (1995) 613.
- [26] J. Barzilai, J.M. Borwein, *IMAJ Numerical Analysis* 8 (1988) 141.
- [27] A.X. Cong, G. Wang, *Optics Express* 13 (2005) 9847.
- [28] W. Cong, G. Wang, D. Kumar, Y. Liu, M. Jiang, L.V. Wang, E.A. Hoffman, G. McLennan, P.B. McCray, J. Zabner, A. Cong, *Optics Express* 13 (2005) 6756.
- [29] G. Alexandrakis, F.R. Rannou, A.F. Chatziioannou, *Physics in Medicine and Biology* 50 (2005) 4225.
- [30] S. Zhu, J. Tian, G. Yan, C. Qin, J. Feng, *International Journal of Biomedical Imaging* 2009 (2009) 960573.
- [31] X. Chen, X. Gao, D. Chen, X. Ma, X. Zhao, M. Shen, X. Li, X. Qu, J. Liang, J. Ripoll, J. Tian, *Optics Express* 18 (2010) 19876.
- [32] T.J. Rudge, V.Y. Soloviev, S.R. Arridge, *Optics Letters* 35 (2010) 763.
- [33] A. Zacharopoulos, A. Garofalakis, J. Ripoll, S. Arridge, *Journal of Physics: Conference Series* 255 (2010) 012006.
- [34] W. Yin, S. Osher, D. Goldfarb, J. Darbon, *SIAM Journal of Imaging Sciences* 1 (2008) 143.